Pore-scale simulations for a Geothermal Reservoir under lithostatic pressure and different tail water injection scenarios

Rita Mwendia Njeru[1], *Matthias* Halisch[2 *], *Arne* Jacob[3], *Andreas* Weber[3], *János* Szanyi[1]

[1]University of Szeged, Department of Mineralogy, Geochemistry and Petrology, Egyetem street 2, 6722 Szeged, Hungary
[2]LIAG Institute for Applied Geophysics, Stilleweg 2, D-30655 Hannover, Germany
[3]Math2Market GmbH, Richard-Wagner-Straße 1, D-67655 Kaiserslautern, Germany

Abstract. Geothermal energy is a promising renewable energy source, considering the high costs of fossil energy and the need to reduce greenhouse gases drastically. Being a crucial energy source for the energy transition worldwide, the exploration and development of geothermal resources have become increasingly important. The Dunántúli Group (DG), located in the Hungarian part of the Pannonian Basin, stands out as being most promising for geothermal energy production. Currently, over 600 operational wells targeting the DG exist in Hungary. It is proposed to drill 2 injection wells for 1 production well in this reservoir, but only 5% of the total wells are used for reinjection purposes. Limited knowledge exists about microscale pore structures and flow properties of this formation, crucial for both, successful water reinjection and for geothermal energy extraction. Severe clogging processes afflict geothermal wells in this region, shutting down injection wells within a short amount of time, causing significant extra costs and delays in progressing Hungary´s energy transition.

The first part of this study [1] (presented at the 2024 SCA Symposium) investigated selected reservoir samples from the DG. Classical mineralogical and petrophysical methods, an extensive core-flooding program for controlled clogging of artificial and natural core samples, as well as X-ray µ-CT imaging, qualitative and quantitative 3-D image analysis, and pore scale simulations with special focus upon the physical pore clogging have been utilized. As highlighted, storage properties are favorable, and the pore throats, which control fluid flow, are nearly of the same size as the movable particles within the pore-system. This fact, coupled with smaller particles present in the re-injection fluid, leads to significant and deep-seated clogging of flow pathways.

In the second phase of this ongoing project, we simulated the effects of lithostatic stress and varying injection pressures on pore geometry and flow properties using digital rock models. Since the permeable part of the DG lacks cementation, or part of the cement has leached out during previous processes, excessive reinjection pressures may lead to formation compaction, reducing pore throat size and progressively clogging the entire injection zone. Using our newly developed workflow in GeoDict, we can simulate various reinjection scenarios, improving the understanding of clogging mechanisms and optimizing tail water reinjection strategies. These insights will significantly advance the understanding of fluid transport in the DG and support stakeholders in developing more efficient and sustainable reinjection wells.

* Corresponding author: matthias.halisch@liag-institut.de

1 Introduction

The global energy transition necessitates the accelerated deployment of renewable energy resources in order to reduce dependence on fossil fuels and to mitigate the impacts of climate change. Among renewable energy sources, geothermal energy occupies a distinctive position due to its capacity to deliver uninterrupted baseload power, irrespective of independent of weather and time of day [2].

Geothermal systems offer high capacity factors and long operational lifetimes, making them critical in achieving net-zero energy targets outlined in international climate agreements [3].

The exploration and exploitation of deep geothermal reservoirs have intensified in recent years, particularly in sedimentary basins where permeability supports large-scale production without the need for stimulation [4]. However, sustaining production from geothermal systems critically depends on the successful reinjection of produced water. Reinjection serves to maintain reservoir pressure, dispose of spent brine, and enhance the long-term sustainability of the resource [5]. Despite its importance, reinjection practices are frequently hampered by clogging phenomena within the reservoir formation [6]. Physical clogging by suspended solids or mobilized fines causes rapid injectivity decline, challenging operations and economics [1, 7].

In porous media reservoirs such as those found in the Pannonian Basin, the risk of physical clogging is accelerated by the presence of fine-grained sediments and the generally unconsolidated nature of the sandstone formations [8]. The tail waters from geothermal production typically carry particulate matter originating from corrosion products, scale precipitates, or formation fines, all of which can accumulate and obstruct pore spaces during reinjection [9]. Understanding the microstructural controls on clogging, particularly the relationship between pore throat sizes and particulate matter dimensions, is therefore essential for designing effective and sustainable reinjection strategies.

Traditional clogging mitigation strategies, including mechanical cleaning, acid stimulation, and filtration upgrades, have had only limited success because they often address symptoms rather than root causes at the pore scale [10]. A deeper, pore-scale related understanding of clogging mechanisms is increasingly recognized as essential. Digital rock physics simulations, coupled with realistic lithostatic and injection stress scenarios, offer promising pathways to predict clogging behavior under operational conditions and to design sustainable reinjection strategies [11, 12, 13, 14].

Recent advances in digital rock physics, combined with high-resolution X-ray micro-computed tomography (μ-CT) and pore-scale modeling, enable a detailed investigation of flow and transport phenomena under realistic subsurface conditions [11, 12, 13]. These techniques allow the simulation of lithostatic stress impacts, dynamic clogging processes, and injection pressure variations on pore network structures, providing insights that were previously inaccessible through laboratory experiments alone [14].

While clogging has been addressed in previous work [1], this study focuses on the flow response of the Dunántúli Group (DG) sandstone under lithostatic and injection-induced stress conditions, providing a digital simulation-based assessment of injectivity evolution during operation. The DG, a revised lithostratigraphic unit encompassing the Újfalu and Zagyva Formations, comprises the most intensively utilized geothermal reservoir system in Hungary [15, 16]. We aim to improve the understanding and management of reinjection operations in porous, weakly consolidated sedimentary systems. Insights will contribute to optimizing reinjection practices not only in the Pannonian Basin but also in similar sedimentary geothermal systems worldwide.

2 Geological Background

The Pannonian Basin is a Miocene back-arc basin formed by tectonic subsidence following the uplift of the surrounding Alpine–Carpathian–Dinaric orogens. Over 7000 m of clastic sediments were deposited in this isolated basin, forming extensive aquifers and geothermal reservoirs [17, 18, 19, 20, and 21].

Deposited in a delta-to-alluvial plain system, the Újfalu and Zagyva Formations of the DG consist of poorly consolidated sandstones, siltstones, and clay layers [1, 22]. The Újfalu Formation dominates geothermal production, with sandstone-rich sequences up to 1000 m thick and porosity between 27–31% and permeability ranging from 60–400 mD [23, 24]. However, the sand layers are separated by clayey deposits ranging from a few centimetres to several metres thick, sometimes with a porosity of less than 10%. The overlying Zagyva Formation and Quaternary sediments form a finer-grained, hydraulically distinct cap. The entire DG sequence is part of a gravity-driven flow regime recharged from basin margins, while deeper zones are overpressured due to compaction [25].

The DG's weak cementation and abundant mobile grains contribute to mechanical instability during

reinjection, making it susceptible to clogging and compaction-induced permeability loss [8, 26]. Although more than 600 production wells have been drilled, <5% serve reinjection purposes due to rapid injectivity decline [16, 27].

The Szentes region, with its high-permeability sandstones, serves as a reference site for investigating reinjection-related clogging in Neogene geothermal reservoirs across Central and Eastern Europe.

This formation behavior under stress is further aggravated by poorly sorted textures and the presence of swelling clays, especially in zones of variable diagenesis. In addition to particle-induced clogging, regional tectonic compression and long-term burial-related compaction have also been shown to progressively reduce porosity and permeability in the deeper sequences of the Pannonian Basin [25, 28]. These compaction trends, observed basin-wide, further constrain injectivity during reinjection and must be considered alongside pore-scale mechanisms.

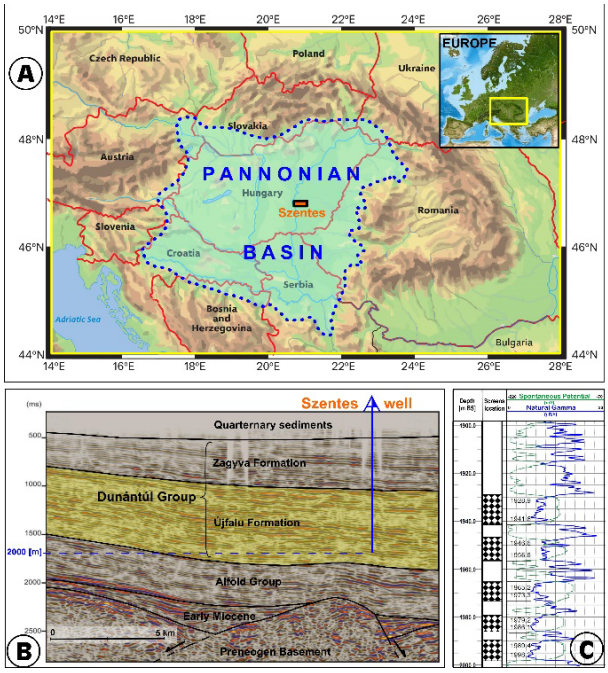

Figure 1. A) Location of the Pannonian Basin with study site; B) Interpreted seismic section in the region of Szentes showing the location of the well being investigated; C) Geophysical log of the studied well as shown in [1].

3 Methods & Sample Material

3.1 Methods

Buoyancy Method. Effective porosity and grain density of the sandstone samples have been determined by the buoyancy method [29]. All samples have been saturated for at least 12h under a high quality vacuum within a special desiccator. As saturation fluid, degassed brine was used. The fluid density was presumed as constant.

Gas Permeability. Gas permeability was measured using a custom-built steady-state permeameter under ambient conditions, featuring a special so-called Fancher-type core sleeve. This device was specifically designed for lower overburden pressures (here: 10 bar = 145 psi) in order to cause less mechanical influence upon brittle and less cemented samples [30], but also features high sealing potential for preventing boundary flow.

µ-CT Imaging. The 3-D imaging has been performed with a high-resolution X-ray computed tomography (µ-CT) system (nanotom M 180, Baker Hughes Waygate). This device is equipped with a special water-cooled nanofocus X-ray tube (180 kV, 20 W) and a large, water-cooled detector (9 MPx, 12 ms) with a high contrast-to-noise ratio (typically better than 10000:1), available at LIAG (Hannover, Germany). For this study, small samples with diameters of about 8 mm have been cut from the larger core plugs, after the routine core analysis. A resolution of 1.5 µm was chosen to resolve cement bridges and pore throat geometry relevant for mechanical modeling. More details about the scanning procedure can be found amongst others in [31, 32]. The digital image analysis and pore scale modelling was conducted using GeoDict digital rock physics toolbox [14].

3.2 Sample Material

For any systematic studies of either processes or application based scenarios, always a sufficient amount of core material is needed. But without the neccessity to reinject thermal fluids by law, and by also knowing the DG formation is a very productive reservoir, literally no cores are taken during drilling operations, to avoid these extra costs. For this study, core plugs from the only publically available drilled core have been prepared for a basic analysis.

For our study, representative sandstone core samples extracted from a depth between 1936 m and 1960 m in the DG were studied. The core samples were cut from 8 m of the drill core to obtain samples of 37 mm in diameter and height. Several samples have been used for the previous study [1], covering the main features and structures of the DG important for a successful reinjection of fluids. Sample preparation was carried out at the GeoChem Limited laboratories, Hungary (https://geochem-ltd.eu//). The samples feature coarse, medium, and fine sand grains, respectively. They exhibit varying degrees of cementation, scaling with their porosity (lower porosity equals higher cementation,

higher porosity equals lower cementation). X-ray diffraction analysis revealed that the main component for all samples is quartz, followed by feldspars, mica, and non-swelling clay minerals (according to XRD-results: 45-60 w.-% SiO2; 20 w.-% feldspars, mostly plagioclase; 7 w.-% muscovite; 10 w.-% chlorite; 3 w.-% kaloninite; 9-20 w.-% CaCO3; 1 w.-% residuals).

The petrophysical measurements have been challenging to perform, due to the unconsolidated nature of the rock samples. Nevertheless, it was possible to derive reproducible and hence reliable data for a general characterization. The effective porosity is high, ranging from approx. 27% - 31 %, and are in good accordance with the degree of cementation that has been visually detected. Gas-permeability follows this trend, ranging from about 60 mD for the 27% porosity sample, to 400 mD for the 31% porosity sample. Remarkably, a significant permeability increase was observed in between porosity ranges from 28 – 29%. This might indicate a crucial pore throat size change, dominating the flow properties and hence most likely physical clogging processes as well. Figure 2 shows a representative 2D µ-CT image and the according core plug.

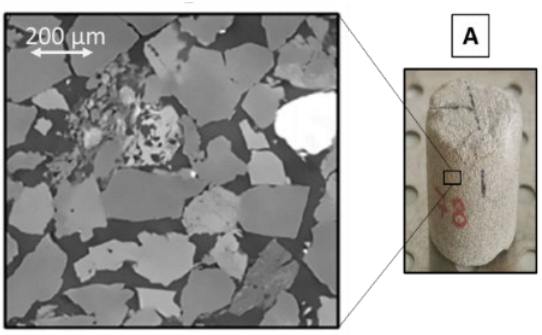

Figure 2. Representative 2D µ-CT image and according core plug of the DG used for this study.

4 Pore Scale Simulations

The pore scale simulations have been performed with the GeoDict digital material laboratory software, developed and distributed by [14]. 3D micro-CT images, derived at a voxel resolution of approximately 3µm have been processed as described by [1, 32] and cropped to digital volumes with approximately 1000^3 voxels (2.5-3.0 mm length) ensuring at least some representativeness of the pore structure. To simulate the influence of different injection conditions within the digital cores, a multi-step simulation workflow was applied to each geometry as follows. Please note that this study primarily aims to explore process understanding and relative trends across different injection scenarios. Consequently, no explicit REV (Representative Elementary Volume) check was performed, as absolute representativeness of porosity and permeability was not the primary focus at this stage.

4.1 Flow Simulations

The Navier-Stokes-Brinkman equations (Eq. 1) are used in the filtration simulations to compute the fluid flow [33, 34]. Due to the creeping flow through the pores, the equations are usually simplified to the Stokes equations by dropping the nonlinear (inertia) term (remark: our assumption for being in creeping flow regime holds, as we are on average well below the Reynolds numbers that indicate turbulent flow for this characteristic length-scale. In porous media, a critical Reynolds number typically lies around 10 to 100. In this case, the Reynolds number is 6.1265e-10 for a characteristic length of 4.257e-07 m. We also neglect the Brinkman term in this work, since we do only track particles with a size larger than a voxel. If a particle deposits within a pore, the corresponding voxels are blocked for any further flow and considered as 'solid' material. Only fully open or fully closed voxels are considered; partially filled voxels are not used in either flow or collision calculations to maintain numerical consistency and phase distinction:

$$\mu \Delta u - \rho(u \cdot \nabla) u - \mu \kappa^{-1} u = \nabla p \text{ on } \Omega, \qquad \text{(Eq. 1)}$$

$$\text{with } \nabla \cdot u = 0 \text{ on } \Omega,$$

$$\text{and } u = 0 \text{ on } \Gamma,$$

where Ω = numerical domain, u = velocity, p = pressure, μ = dynamic viscosity, Γ = solid surface, ρ = density, κ = porous voxel permeability.

4.2 Mechanical Simulations

The effective mechanical properties are computed using homogenization method [35] as implemented in the ElastoDict [36]. The module utilizes an iterative Fast-Fourier-Transformation solver (FFT) [37] to compute the response of a voxelized microstructure subjected to macroscopic strain. The solution involves the following system of equilibrium (Eq. 2) and kinematic (Eq. 3) partial differential equations:

$$\nabla \cdot (\sigma(\varepsilon)) = 0 \qquad \text{(Eq. 2)}$$

$$\varepsilon = E + \frac{1}{2}(\nabla u + (\nabla u)^T) \qquad \text{(Eq. 3)}$$

Here, E denotes the macroscopic strain tensor and u the displacement vector. After solving for the local stress σ and strain tensors ε, volume averaging over the 3D domain results to the effective stiffness tensor. Following the mechanical simulation, bulk density and porosity,

additional seismic recalculations were executed for each rock sample.

4.3 Other DRP Simulations

MICP Simulations. Capillary pressure (Pc) curves were modeled using the PoroDict module within the GeoDict software suite [14], based on high-resolution 3D digital rock volumes. The simulations rely on morphological algorithms that analyze the pore-throat network topology and compute drainage and imbibition curves using a non-wetting phase invasion method. From these curves, effective pore throat radius distributions were derived via the Washburn equation, allowing for quantitative characterization of capillary entry pressures and connectivity. This approach enables a robust link between 3D pore space geometry and multiphase flow behavior, supporting detailed interpretation of wettability, saturation history, and pore accessibility relevant for reservoir quality assessment from a digital core perspective.

Pore Sizes. Pore size distributions were determined using the Identify Individual Pores tool within GeoDict [14], which segments the connected pore space into individual pore bodies based on 3D watershed algorithms. For each identified pore, geometric parameters such as equivalent diameter, pore volume, and surface area were computed. The resulting statistics were exported via SurfaceArea output files, enabling the derivation of representative pore size histograms and cumulative distributions. This workflow provides a direct link between segmented µ-CT data and quantitative pore geometry.

5 Results

5.1 Results from uncompressed state

The results presented in this section have previously been discussed in [1]. They describe the reservoir conditions without lithostatic stress and in the absence of active injection. For completeness with our study, we re-use these results for a comparison with the new findings. The simulated total porosity of the sandstone sample was 10.74%, with 9.91% of the pore volume being connected. Non-accessible porosity accounted for 0.68%, and dead-end pores contributed 0.59% to the total. The through-porosity—defined as the fraction of the pore space supporting continuous flow—was calculated at 9.32%. Please note that the digital datasets are not representative with respect to absolute porosity or permeability values due to computational limitations. However, as this study focuses on the conceptual understanding of scenario-dependent trends, relative changes remain valid for interpretative purposes.

Since fluid flow, and hence the infiltration of particles into the samples, is dominated by the narrowest pore within the widest flow path, i.e,. by the pore throats of the pore networks, results from digital MICP simulations, combined with results from the permeability development during the clogging simulation are shown first. Spatial particle agglomerations as well as infiltration depths for the DRP datasets are highlighted afterwards. Please note that due to the higher image resolution, resulting numerical domains are much smaller than the coarser scans performed for the general assessment of the laboratory experiments, which explains the "spiky" distribution in the simulated MICP in Figure 3. Nevertheless, knowing that absolute numbers might not be representative, we were mainly interested in where and why the clogging happens, and if we generally can reproduce the macroscopic observations regarding infiltration depth.

Figure 3 displays the results of the MICP simulations before (Figure 3, blue line) and after (Figure 3, red line) the digital clogging. The dashed red line indicates changes in between. The overall reduction of volume fraction for pore throat diameters is homogeneously distributed. Nevertheless, two favorable pore throat diameter ranges can be observed: from 30-35 µm and from 35 – 40 µm. The reduction can be related to the clogging of flow paths within the domain. We do not observe an increase in smaller pore throats. In fact, the remaining throats in between these areas are remarkably constant and undisturbed, possibly indicating a very homogenous and "tight" packing of clogged particles.

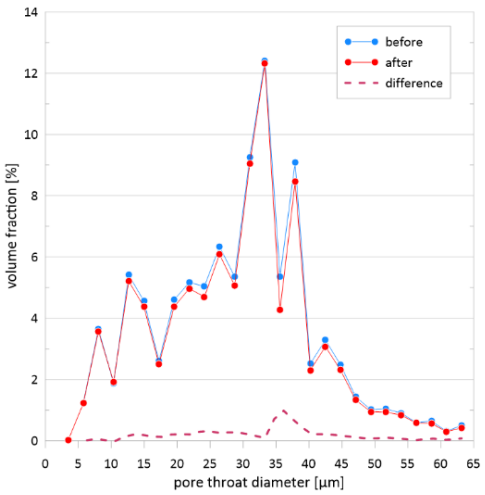

Figure 3. Results of the MICP simulations for the natural sample, before (blue line) and after (red line) digital clogging. The dashed red line displays the difference of both curves.

As described by [1] overall change in porosity is not very remarkable, but at least constantly decreases during the simulation. Additionally, permeability decrease over time is not very pronounced and follows a pretty constant, i.e., decreasing trend. This result facilitates the assumption in the first stage of our study as presented in 2024 that the clogging of particles obviously happened homogeneously, i.e., less locally clogged areas within the digital sample exist, leading to this result.

Our previous investigations [1] demonstrated that under simplified digital clogging scenarios, particle deposition tended to occur predominantly near the inflow region, leading to a relatively homogeneous blockage of pore space. These findings were associated with only minor variations in local flow velocities and indicated a shallow infiltration depth of particulate matter - typically limited to less than one-third of the total sample length. While these earlier results did not show pronounced velocity perturbations or deep-seated clogging patterns, they offer a useful reference for the expected qualitative behavior under realistic reinjection conditions. For future work, a degradation in flow performance - reflected by decreasing porosity, permeability, and capillary connectivity - can be anticipated once physical or chemical clogging mechanisms are systematically integrated into the simulation framework. The following sections now explore the impact of lithostatic and injection pressures on the same geometry.

5.2 Results with applied lithostatic pressure

Under lithostatic stress (equal to the in-situ formation depth, here approx. 1200 m b.s.f.) conditions (without active injection), the simulated total porosity of the sandstone sample was 10.74 %, with 9.91 % of the pore volume being connected. Non-accessible porosity accounted for 0.68 %, and dead-end pores contributed 0.59 % to the total. The through porosity - representing pathways supporting continuous flow - was calculated at 9.32 %. Figure 4 gives an impression of the connected porosity (Fig. 4A), connected pathways and flow velocities (Fig. 4B) and pore size distributions (Fig. 4C).

Permeability in the Y-direction (i.e., the in-situ injection direction of the fluid at the well-site) was determined to be 95.06 mD. At an applied pressure drop of 0.02 Pa, the average superficial flow velocity within the sample was computed as 5.98×10^{-10} m/s. The pore throat size distribution, derived from digital mercury injection capillary pressure (MICP) simulation (Figure 5), revealed a dominant peak around 35 µm, with a steep decline toward larger diameters. The highest volume fraction exceeded 17 %, indicating a significant share of the pore network is controlled by moderately narrow constrictions. Volume fractions dropped rapidly for throat diameters above 50 µm, confirming that flow-relevant transport remains governed by the finer-scale throat geometry.

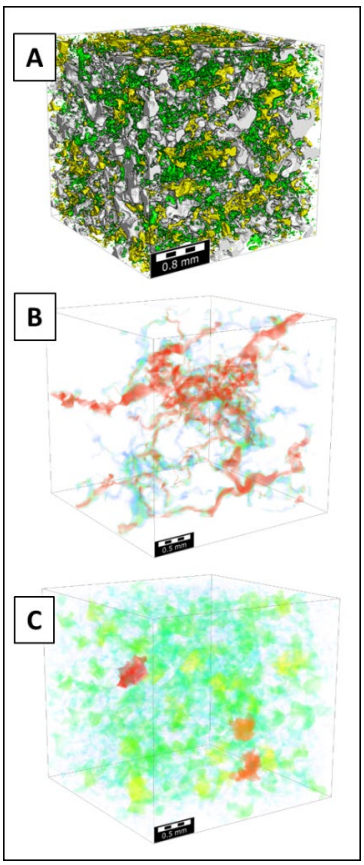

Figure 4. 3D visualization of the digital rock geometry after application of simulated lithostatic pressure. (A) Connected pore space, color-coded by local connectivity; (B) Flow streamlines illustrating principal flow pathways; (C) Pore size distribution mapped onto the pore space, color-coded by equivalent pore diameter.

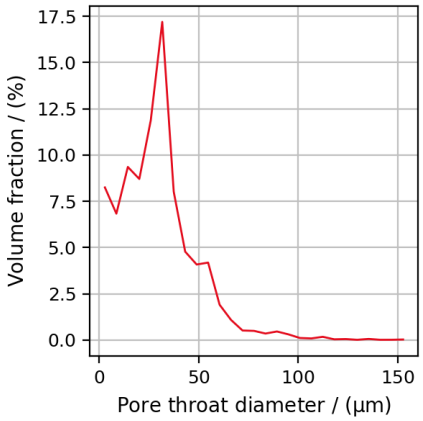

Figure 5. Simulated pore throat size distribution derived from digital mercury intrusion capillary pressure (MICP) analysis of the geometry under lithostatic loading conditions. The data reflect the relative volume contribution of throat diameters across the connected pore network

5.3 Results with low injection pressure

Under low-pressure injection conditions (25 bar), the digital rock simulations yielded a total porosity of 10.65 %, with a connected porosity of 9.48 %. The difference between connected and total porosity reflects a non-accessible fraction of 1.17 %, while dead-end pores accounted for 1.07 %. The through porosity, was determined to be 8.41 %.

Permeability in the principal injection flow direction (Y-axis) was calculated at 91.41 mD. The corresponding mean flow velocity within the connected pore network was 5.99×10^{-10} m/s.

The pore size distribution (Figure 6) , based on segmented pore body volumes, showed a broad peak centered between 80 µm and 160 µm in intermediate fit diameter, with maximum relative volume probability around 0.025. The distribution is moderately skewed toward smaller pore bodies but retains a long tail toward larger diameters above 300 µm.

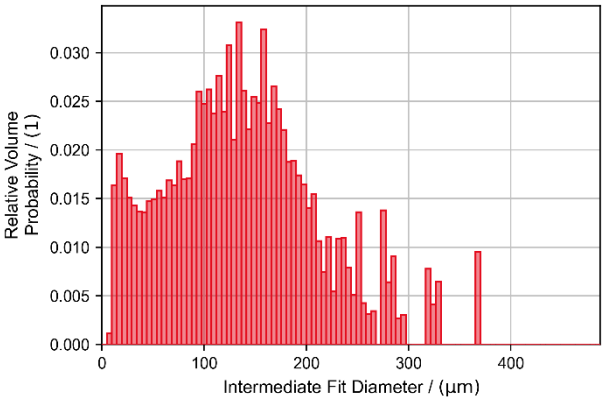

Figure 6. Pore size distribution derived from digital image analysis of the geometry under lithostatic loading conditions and for low injection pressure (25bar).

The pore throat diameter distribution (Figure 7) exhibited multiple peaks below 50 µm, with the most prominent maxima near 10 µm and 35 µm. Volume fractions sharply decrease for throat diameters beyond 50 µm, indicating that the majority of fluid connectivity is governed by relatively narrow constrictions.

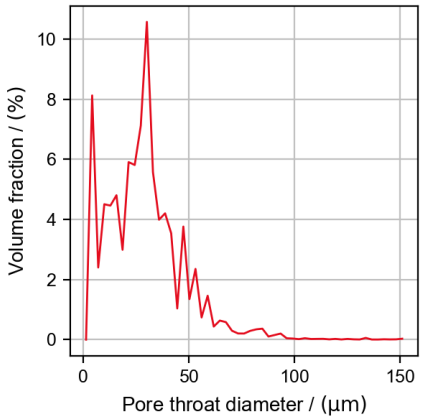

Figure 7. Simulated pore throat size distribution derived from digital mercury intrusion capillary pressure (MICP) analysis of the geometry under lithostatic loading conditions and for low injection pressure (25bar). The data reflect the relative volume contribution of throat diameters across the connected pore network.

5.4 Results with high injection pressure

Under high-pressure injection conditions (75 bar), digital simulations indicated a total porosity of 10.43 %, with 9.27 % of the pore volume being connected. The proportion of non-accessible porosity remained at 1.17 %, while dead-end porosity was determined to be 1.05 %. Through porosity was calculated as 8.22 %, suggesting a slightly lower continuous flow fraction compared to the low-pressure case.

The simulated permeability in the principal injection flow direction (Y-axis) was 81.12 mD, with a mean flow velocity of 5.33×10^{-10} m/s through the connected pore network. The pore size distribution (Figure 8) exhibited a dominant population of intermediate fit diameters between 80 µm and 160 µm, with relative volume probabilities peaking around 0.027. A long tail extending beyond 300 µm was again observed, indicating a broad pore body spectrum.

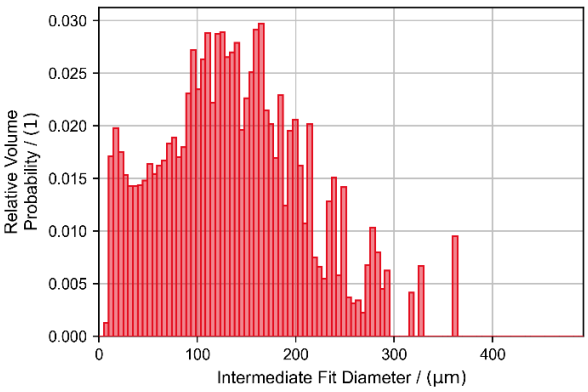

Figure 8. Pore size distribution derived from digital image analysis of the geometry under lithostatic loading conditions and for high injection pressure (75bar).

Pore throat diameters (Figure 9) show prominent peaks below 50 µm, with the main maxima near 10 µm and 35 µm. The overall volume fraction associated with narrow throats was slightly higher than in the low-pressure scenario, with a maximum exceeding 12 %. This indicates that flow is still primarily governed by small-scale pore throat constrictions.

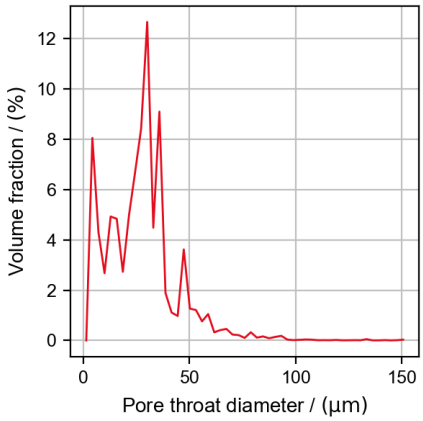

Figure 9. Simulated pore throat size distribution derived from digital mercury intrusion capillary pressure (MICP) analysis of the geometry under lithostatic loading conditions and for high injection pressure (75bar). The data reflect the relative volume contribution of throat diameters across the connected pore network.

5.5 Comparison and Impact on Injection

A comparison of lithostatic, low-pressure (25 bar), and high-pressure (75 bar) injection scenarios reveals systematic trends in permeability, flow behavior, and pore throat sizes. Under lithostatic conditions, the permeability was 95.06 mD and the average flow velocity was 5.98×10^{-10} m/s. As injection pressure increased, both permeability and flow velocity slightly declined: at 25 bar, permeability was 91.41 mD and velocity remained constant at 5.99×10^{-10} m/s, while at 75 bar, values decreased to 81.12 mD and 5.33×10^{-10} m/s, respectively.

Simultaneously, pore throat diameters showed a shift under varying stress conditions. Under lithostatic stress, the majority of pore throat diameters were concentrated below 50 µm, with prominent peaks at approximately 10 µm and 35 µm, which directly correlates with the higher permeability and flow rates. As the injection pressure increased, the pore throat diameter distribution shifted towards smaller values, with a larger fraction of narrower throats (below 50 µm) observed, particularly under the high-pressure conditions (75 bar). This reduction in pore throat size corresponds with the observed decline in permeability and flow velocity, confirming that increased injection pressure leads to pore compaction, restricting flow paths and reducing overall fluid mobility. These results suggest that the reduction in permeability is directly linked to the compression and narrowing of pore throats, which limits the available flow pathways. As the pore structure becomes more constrained under higher injection pressures, the system experiences greater resistance to flow, resulting in lower flow velocities and permeability. This highlights the importance of pore geometry in determining flow behavior under injection scenarios, and provides critical insights for optimizing reservoir performance under varying stress conditions.

The presented injection scenario simulations highlight that even in the absence of chemical or particulate clogging, mechanical stress alone—through lithostatic and injection-induced compression—can significantly reduce permeability and narrow pore throats, thereby restricting flow. When combined with known clogging mechanisms such as particle intrusion or mineral precipitation, this dual effect can amplify rapidly, leading to severe injectivity loss. In fact, operational evidence from several geothermal sites in Hungary has shown that reinjection wells in the DG reservoir often become unserviceable within one to two years after commissioning. These findings underscore the importance of an integrated assessment approach that accounts for both physical clogging risks and stress-driven transport evolution. The conclusions below summarize how the applied digital workflow supports this objective and contributes to a more resilient reinjection strategy.

6 Conclusions

Based on a combined laboratory and digital analysis of the Dunántúli Group reservoir sandstones, this study demonstrates how integrated workflows can improve our understanding of injectivity behavior under realistic subsurface conditions.

The following key findings summarize the insights gained from classical core analysis, 3D pore structure imaging, and pore-scale simulation of flow scenarios.

- The heterogeneous DG reservoir sandstones exhibit favorable porosity and permeability conditions for geothermal production, but are highly susceptible to clogging due to weak cementation and a pore throat network closely matching the size of suspended particles in reinjection fluids.
- Classical petrophysical methods, combined with high-resolution µ-CT imaging, enable reliable characterization of pore geometry and grain-scale

cementation, even in unconsolidated, brittle core samples.

- Digital rock physics simulations, calibrated with laboratory results, provide a powerful tool to investigate flow and mechanical behavior of the reservoir under varying stress regimes and injection scenarios.
- The integration of effective porosity and permeability measurements, 3D structural imaging, and digital modeling facilitates scenario-based evaluation of injectivity evolution, supporting optimized reinjection strategies for weakly consolidated sandstone reservoirs.
- Simulations under increasing injection pressure (25 and 75 bar) revealed a systematic compaction of the pore network, with through porosity and permeability decreasing up to 15 % relative to the lithostatic baseline, and narrowing of flow-governing pore throats.
- The combined influence of lithostatic compaction and particulate clogging was shown to affect not only porosity but the functional connectivity of the pore space, suggesting that injectivity failures may be driven by subtle geometric changes that precede any chemical alteration or scaling effect.

The developed workflow (Figure 10) integrates classical laboratory methods (CAL/SCAL), high-resolution µ-CT imaging, and digital rock physics (DRP) to systematically evaluate reservoir rock behavior under varying injection scenarios. While CAL/SCAL deliver reference measurements for permeability, capillary pressure, and clogging potential, µ-CT imaging provides the geometric basis for both experimental validation and virtual analysis. Digital simulations build upon these inputs to explore the effects of lithostatic stress, injection pressure, and fluid-mineral interactions across different operational regimes. This multi-scale, hybrid approach enables scenario-based modelling of injectivity evolution and supports improved reservoir development strategies.

7 Outlook

Building on the modeling framework established in this study, future work will expand the scope of injection scenario simulations to include a broader range of operational parameters and geological conditions. This includes the systematic variation of injection pressure, rate, and cycling strategies, as well as the implementation of anisotropic boundary conditions to better reflect in-situ stress fields and directional permeability. In addition, extending the analysis to other lithologies within the reservoir system - especially more strongly cemented or clay-rich facies - will provide further insight into material-specific injectivity behavior.

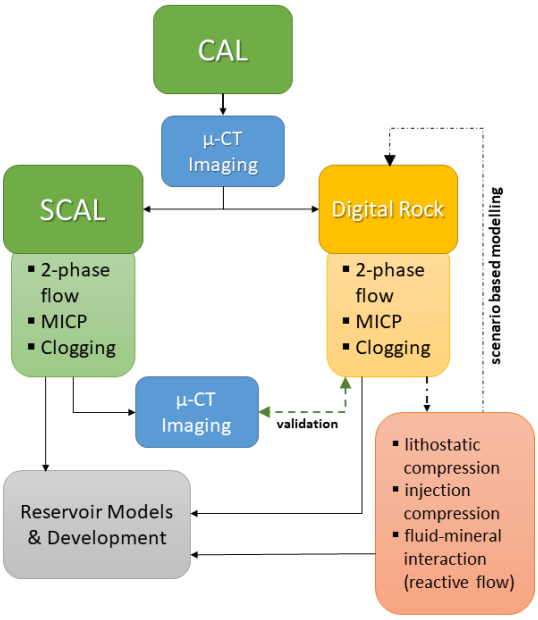

Figure 10. Integrated workflow combining CAL/SCAL, µ-CT imaging, and digital rock physics to assess flow and injectivity under different injection scenarios. Digital simulations extend physical measurements through scenario-based modelling of stress, compression, and reactive transport.

A key future component will also be the integration of reactive transport modeling to assess the dynamic interaction between geochemical alteration and mechanical pore evolution over time. This will enable the digital workflow to not only characterize but also predict the coupled effects of stress, structure, and chemistry - thereby improving the long-term management of reinjection performance in complex geothermal systems.

Acknowledgments

This study builds on prior collaborative work between institutions including the University of Szeged, LIAG, Math2Market GmbH, and Geochem Ltd., and we acknowledge all co-authors and partners from phase 1 od the study whose insights and datasets laid the foundation for the current research. Special appreciation goes to the SCA´s Technical Board for reviewing and improving this manuscript.

References

[1] R.M. Njeru, M. Halisch, A. Jacob, A. Weber, P. Koroncz, F. Fedor, J. Szanyi, Int. Symp. Soc. Core Analysts, SCA2024-1014 (2024a)

[2] J.W. Lund, A.N. Toth, Geothermics **90**, 101915 (2020)

[3] International Energy Agency, *Net Zero by 2050: A Roadmap for the Global Energy Sector*, IEA, Paris (2021)

[4] I. Sass, A.E. Götz, Terra Nova **24**, 142–147 (2012)

[5] R. Shortall, B. Davidsdottir, G. Axelsson, Renew. Sustain. Energy Rev. **44**, 391–406 (2015)

[6] W. Luo, A. Kottsova, P.J. Vardon, A.C. Dieudonné, M. Brehme, Renew. Sustain. Energy Rev. **185**, 113623 (2023)

[7] J. Szanyi, T. Medgyes, B. Kóbor, E. Pál-Molnár, GeoLitera, Univ. Szeged (2015)

[8] Á. Markó, M. Tóth, M. Brehme, J. Mádl-Szőnyi, EGU Abstracts, https://doi.org/10.5194/egusphere-egu23-6992 (2021)

[9] J. Xia, H. Tian, B. Dou, P. Xiao, J. Zheng, X. Lai, J. Hydrol. **625**, 130066 (2023)

[10] G. Axelsson, EPJ Web Conf. **50**, 02001 (2013)

[11] H. Andrä, N. Combaret, J. Dvorkin, E. Glatt, J. Han, M. Kabel, Y. Keehm, F. Krzikalla, M. Lee, C. Madonna, M. Marsh, T. Mukerji, E.H. Saenger, R. Sain, N. Saxena, S. Ricker, A. Wiegmann, X. Zhan, Comput. Geosci. **50**, 25–32 (2013a)

[12] H. Andrä, N. Combaret, J. Dvorkin, E. Glatt, J. Han, M. Kabel, Y. Keehm, F. Krzikalla, M. Lee, C. Madonna, M. Marsh, T. Mukerji, E.H. Saenger, R. Sain, N. Saxena, S. Ricker, A. Wiegmann, X. Zhan, Comput. Geosci. **50**, 33–43 (2013b)

[13] M.J. Blunt, B. Bijeljic, H. Dong, O. Gharbi, S. Iglauer, P. Mostaghimi, A. Paluszny, C. Pentland, Adv. Water Resour. **51**, 197–216 (2013)

[14] Math2Market GmbH, *GeoDict2024.pdf* (2024)

[15] G. Tari, G. Bada et al., AAPG Bull. **107**, 1391–1417 (2023)

[16] J. Szanyi, B. Kovács, A. Hawkar, in: *The Miocene Extensional Pannonian Superbasin*, Vol. 2: Geoenergy Exploration, Geol. Soc. London (in press, 2024)

[17] I. Almási, J. Szanyi, *Hydrogeology of the Pannonian Basin*, Groundwater Project, Guelph (2024)

[18] I. Bérczi, in: L.H. Royden, F. Horváth (Eds.), *The Pannonian Basin: A Study in Basin Evolution*, AAPG Mem. **45**, (1988)

[19] P. Dövényi, F. Horváth, in: L.H. Royden, F. Horváth (Eds.), *The Pannonian Basin: A Study in Basin Evolution*, AAPG Mem. **45**, (1988)

[20] G. Juhász, G. Pogácsás, I. Magyar, P. Hatalyák, Glob. Planet. Change **103**, 174–192 (2013)

[21] A. Varga, G. Bozsó, I. Garaguly, B. Raucsik, A. Bencsik, B. Kóbor, Geofluids **2019**, 4863814 (2019)

[22] P. Koroncz, Z. Vizhányó, M.P. Farkas, M. Kuncz, P. Ács, G. Kocsis, P. Mucsi, A. Fedorné Szász, F. Fedor, J. Kovács, Energies **15**, 39136 (2022)

[23] A. Bálint, J. Szanyi, Cent. Eur. Geol. **58**, 28–49 (2015)

[24] J. Szanyi, B. Kovács, Geothermics **39**, 357–364 (2010)

[25] J. Tóth, I. Almási, Geofluids **1** (2001)

[26] R.M. Njeru, M. Halisch, J. Szanyi, Geothermics **122**, 103071 (2024b)

[27] N. Rman, L.L. Bălan, I. Bobovečki, N. Gál, B. Jolović, A. Lapanje, T. Marković, D. Milenić, F. Skopljak, Á. Rotár-Szalkai, N. Samardžić, T. Szőcs, D. Šolaja, N. Toholj, A.M. Vijdea, A. Vranješ, Environ. Earth Sci. **79**, 1–12 (2020)

[28] F. Horváth, B. Musitz, A. Balázs, A. Végh, A. Uhrin, A. Nádor, B. Koroknai, N. Pap, T. Tóth, G. Wórum, Geothermics **53** (2015)

[29] API, *Recommended Practices for Core Analysis*, API Publ. (1998)

[30] M. Rieckmann, Erdöl-Erdgas Z. **36**, 36–51 (1970)

[31] M. Halisch, H. Steeb, S. Henkel, C.M. Krawczyk, Solid Earth **7**, 1141–1143 (2016a)

[32] M. Halisch, M. Schmitt, C.P. Fernandes, Int. Symp. Soc. Core Anal., 1–6 (2016b)

[33] S. Linden, A. Wiegmann, H. Hagen, Graph. Models **82** (2015)

[34] S. Linden, L. Cheng, A. Wiegmann, *Specialized Methods for Direct Numerical Simulations in Porous Media*, Math2Market (2018)

[35] H. Moulinec, P. Suquet, Comput. Methods Appl. Mech. Eng. **157**, 69–94 (1998)

[36] L. Burger, S. Rief, A. Widera, B. Planas, *GeoDict 2024 UserGuide: ElastoDict*, Math2Market GmbH (2024)

[37] H. Grimm-Strele, M. Kabel, Comput. Mech. **64**, 1339–1345 (2019)